ARTICLE

Electrochemical analysis of the ASTM F75 alloy at different pH values and temperatures

A. I. Kociubczyk[1] | **C. M. Méndez**[2] | **R. W. Gregorutti**[3] | **A. E. Ares**[1]

[1] Instituto de Materiales de Misiones, IMAM (CONICET-UNaM), Posadas, Misiones, Argentina

[2] Facultad de Ciencias Exactas, Químicas y Naturales, Universidad Nacional de Misiones, Posadas, Misiones, Argentina

[3] Laboratorio de Entrenamiento Multidisciplinario para la Investigación Tecnológica (LEMIT-CICPBA), La Plata, Buenos Aires, Argentina

Correspondence
A. I. Kociubczyk, Instituto de Materiales de Misiones, IMAM (CONICET-UNaM), Félix de Azara 1552, (N3300LQD) Posadas, Misiones, Argentina.
Email: aares@fceqyn.unam.edu.ar

Funding information
CONICET and Agencia Nacional de Promoción Científica y Tecnológica (ANPCyT), Grant numbers: PICT-2014-0170, PICT-2012-2952

The electrochemical behavior of ASTM F75 alloy was analyzed in a sodium chloride solution at pH values of 5, 7, and 9 and temperatures of 37 and 42 °C. The tests were performed in samples corresponding to two different regions of a hip prosthesis. Polarization curves showed that as pH increased the passivity range decreased. However, according to the complementary potentiodynamic–potentio-static–potentiodynamic technique performed, the increase in the anodic current density was due to a change in the chromium oxidation state from Cr^{+3} to Cr^{+6} to form CrO_4^{-2}, and not to localized corrosion. On the other hand, neither the microstructure nor the temperature had influence on the electrochemical response of ASTM F75. The electrochemical impedance spectroscopy test showed that as pH increased, the passive film became more compact and thicker. However, its resistance decreased and the electrical double layer became more disordered, promoting diffusion processes of charged species. These results are in agreement with those obtained in the polarization curves, which showed an increase in the dissolution of the passive film, caused by the change in the chromium oxidation state, as pH increased.

KEYWORDS
ASTM F75, biomaterials, corrosion, pH, temperature

1 | INTRODUCTION

Bioimplants are increasingly being used in reconstructive tissue engineering to improve the life quality of people. In addition, in traumatology, load-bearing implants are used for knee and hip replacement. An important aspect of the alloys used for these purposes is that they must be accepted by the human body without causing adverse effects such as allergy, inflammation, and toxicity. In addition, they should be resistant to corrosion and wear because implant processes promote the release of metallic ions to the tissues, affecting the biocompatibility and the mechanical performance of implants. Corrosion resistance can be affected by the physiological environment of the human body, which is composed of blood and other components as sodium, proteins, minerals, anions (Cl^-, PO_4^{-3}, etc.), cations (Na^+, K^+, Ca^{+2}, etc.) and dissolved oxygen. The balance of corrosion reactions on the bioimplant can be altered by biological molecules because of the consumption of products in the anodic and cathodic reactions. Another factor that should be considered is the pH variation. The human body normally maintains the pH level close to 7.4, but this value can be altered by different circumstances. Accidents, imbalances in the biological system caused by diseases and infections or secretions of inflammatory cells and hematomas could cause variations in the pH between 4 and 9. In addition, after surgery, the pH can vary between 5.3 and 5.6 near the implant.[1–5]

The ASTM F75 cast cobalt alloy is widely used as biomaterial because of its high strength and high corrosion and wear resistances.[6–12] These properties are directly related to the microstructure of the material, which is determined by the manufacturing process. Investment casting (IC)[13] is one of the methods used to elaborate surgical

implants, because of its low cost and because it allows producing devices whose geometry would be difficult to process by hot and cold working, such as knee joint prostheses. The main features to consider in an "as cast" microstructure are the primary and secondary dendritic spacing, and the microsegregation in the interdendritic regions. In IC, these parameters are defined by the temperatures of the melt and the shell mold.[14,15] Furthermore, the presence of oxygen in the atmosphere during the different steps of the casting process promotes the formation of nonmetallic inclusions. These particles can produce mechanical fatigue failures, corrosion, or a combination of both.[16,17] Variation in the macro- and microstructure could result in surface changes that may affect the electrochemical behavior of bioimplants, which depends on various factors such as the size and morphology of the grains, the grain boundary density, the orientation, the dendritic arrangement, the distribution of solute, and the anodic and cathodic behavior of each alloy component.[18–26]

The aim of this study was to evaluate and compare the corrosion resistance through cyclic polarization and electronic impedance spectroscopy (EIS) techniques in different regions of a hip prosthesis made of ASTM F75 obtained by IC. The analyses were performed at acid and alkaline pH, and at two temperatures: 37 and 42 °C.

2 | MATERIALS AND METHODS

2.1 | Casting

A femoral prosthesis made of ASTM F75 was obtained by IC to perform electrochemical analysis. The casting temperature was 1600 °C and, as usual practice of the IC process, the shell mold was heated up to 500 °C to increase its permeability and reduce the thermal gradient of cooling, to improve castability. The chemical composition of the alloy is shown in Table 1.

2.2 | Metallographic analysis

Samples were initially polished with silicium carbide (# 120–2500) and then with 0.05 μm alumina powder suspension. The macro- and microstructure were revealed by means of a ferric chloride saturated solution in hydrochloric acid for 5 min, and then using the same solution with 5% nitric acid for another 5 min. The solidification cell size and dendrite spacing were measured by optical images, using the line

TABLE 1 Chemical composition of the ASTM F75 alloy, in wt %

	Co	Cr	Mo	Ni	Fe
ASTM F75	Bal.	30.0	6.0	<1	<0.7

interception method. Microsegregation was measured by energy dispersive X-ray spectroscopy (EDS).

2.3 | Electrochemical analysis

Cyclic potentiodynamic tests (CPT) were carried out following the ASTM F2129 standard, using a conventional three-electrode cell with the test material as working electrode, a saturated calomel electrode (SCE) as reference and a platinum electrode as auxiliary. Tests were performed using a ZRA GAMRY® potentiostat/galvanostat. The open circuit potential (OCP) was monitored for 1 h and then the potentiodynamic scanning started at −0.100 V/OCP with scan rate of 0.167 mV/s. The sweep was reversed after passing the threshold current density at a value of two decades older than the value at which the current density increases drastically.

EIS measures were obtained after 1 h exposure at OCP. The frequency range was 100 kHz to 1 mHz and the potential amplitude of ±10 mV. For both CPT and EIS, the human environment was simulated with a 0.9 wt% sodium chloride aqueous solution used as electrolyte. Tests were carried out at pH = 5, pH = 7, and pH = 9, and at 37 and 42 °C.

3 | RESULTS AND DISCUSSION

3.1 | Metallographic analysis

Two regions of the femoral prosthesis were analyzed: one corresponding to the distal region (DR) and the other one to the acetabulum proximal region (APR) (Figure 1). Figure 1 also shows the pouring gate through which the liquid enters to fill the cavity corresponding to the prosthesis in the shell mold.

The APR is the region of greatest mass of the femoral prosthesis, and hence, the region of lower cooling rate during solidification. This feature promotes a lower driving force for solidification, represented by the undercooling defined as $\Delta T = T_e - T^*$, where T_e is the equilibrium melting temperature, and T^* is the temperature of the undercooled liquid. According to the fundamentals of solidification, the lower the ΔT, the lower the amount of solidification nuclei, and therefore the greater the solidification cell size. Figure 2 shows the difference of the solidification cell size in the APR and DR, as a consequence of the variation in ΔT.

The microstructure of the alloy consisted of dendrites of high chromium α-fcc, formed as a consequence of the thermal and constitutional undercoolings produced during solidification, which destabilize the solid/liquid interface (Figure 3).
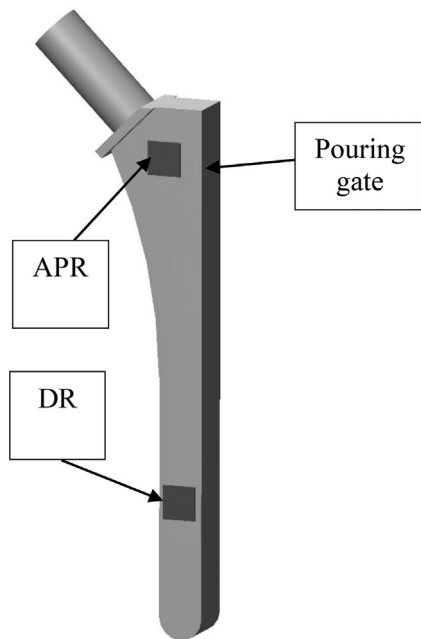
FIGURE 1 Regions of the femoral prosthesis analyzed

As in macrostructures, the dendritic structure is thicker in the APR because of the lower cooling rate in that region, with greater primary and secondary dendritic arm spacing (Table 2).

Another feature to be considered in the microstructure is the microsegregation of the alloying elements, which depends on the partition coefficient k. Elements with $k < 1$ segregate directly towards the last to freeze liquid, while $k > 1$ indicates inverse segregation towards the bulk. The analysis performed by EDS showed that chromium and, particularly molybdenum, segregate directly to the interdendritic regions and that cobalt segregates to the bulk. The concentration of these elements in the APR and DR are recorded in Table 3.

The microsegragation of chromium and molybdenum to the interdendrtic regions is more noticeable in the APR region, as a consequence of the lower cooling rate that reduces the solidification rate, allowing the escape of solute atoms into the liquid.

3.2 | Electrochemical analysis

3.2.1 | Results of cyclic potentiodynamic tests

The susceptibility to localized corrosion was evaluated by cyclic polarization tests. This technique allows evaluating the corrosion potential (E_{corr}), the oxidation state change potential (E_{ox}), and the repassivation potential (E_{rp}). The E_{Corr} is the potential at the open circuit condition, when there is no net current flow; E_{ox} is the polarization level at which the anodic current increases considerably with the applied potential, indicating a change in the oxidation state of the passive film; and E_{rp} is the potential at which the
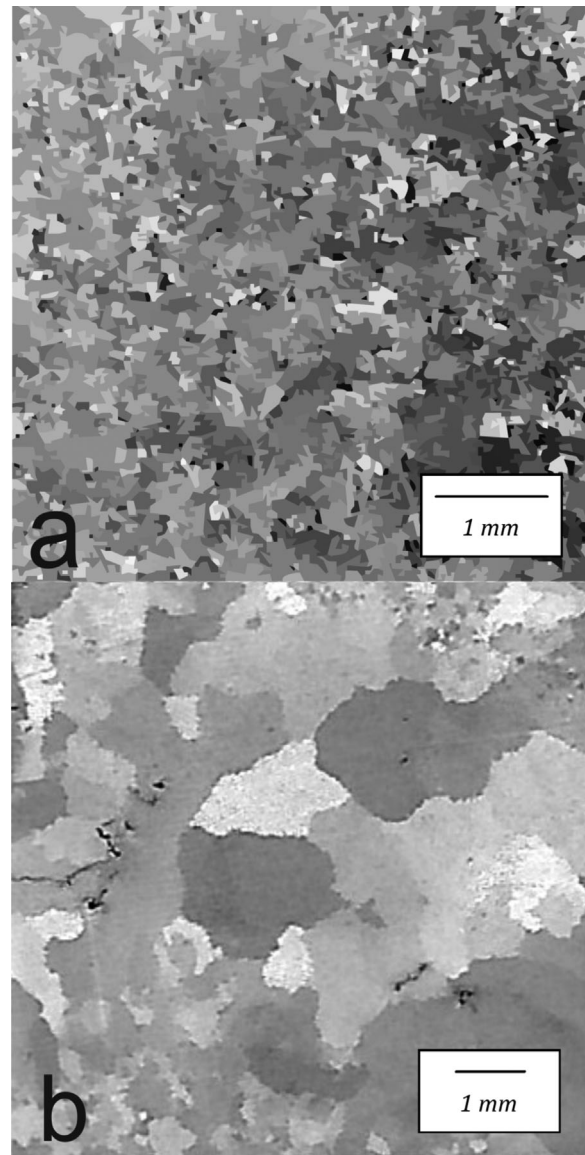

FIGURE 2 Macrographs of ASTM F75 in different regions: (a) Distal region (DR). (b) Acetabulum proximal region (APR)

hysteresis loop is completed upon reverse polarization scan. These parameters are related to the alloys susceptibility to suffer localized corrosion and the capacity for its development. The difference (E_{ox}–E_{corr}) represents the range in which the alloy remains passive. The greater this difference, the lower the susceptibility to localized corrosion.

Figures 4 and 5 show the polarization curves corresponding to the DR and APR regions of the femoral prosthesis, obtained at 37 and 42 °C, for all the pH values evaluated. The values of the electrochemical parameters obtained from the polarization curves are summarized in Table 4.

3.2.2 | Effect of pH

The polarization curves experienced relevant changes with the pH variation. The polarization scan at pH = 5 showed the highest passivity range. The increase in the anodic current
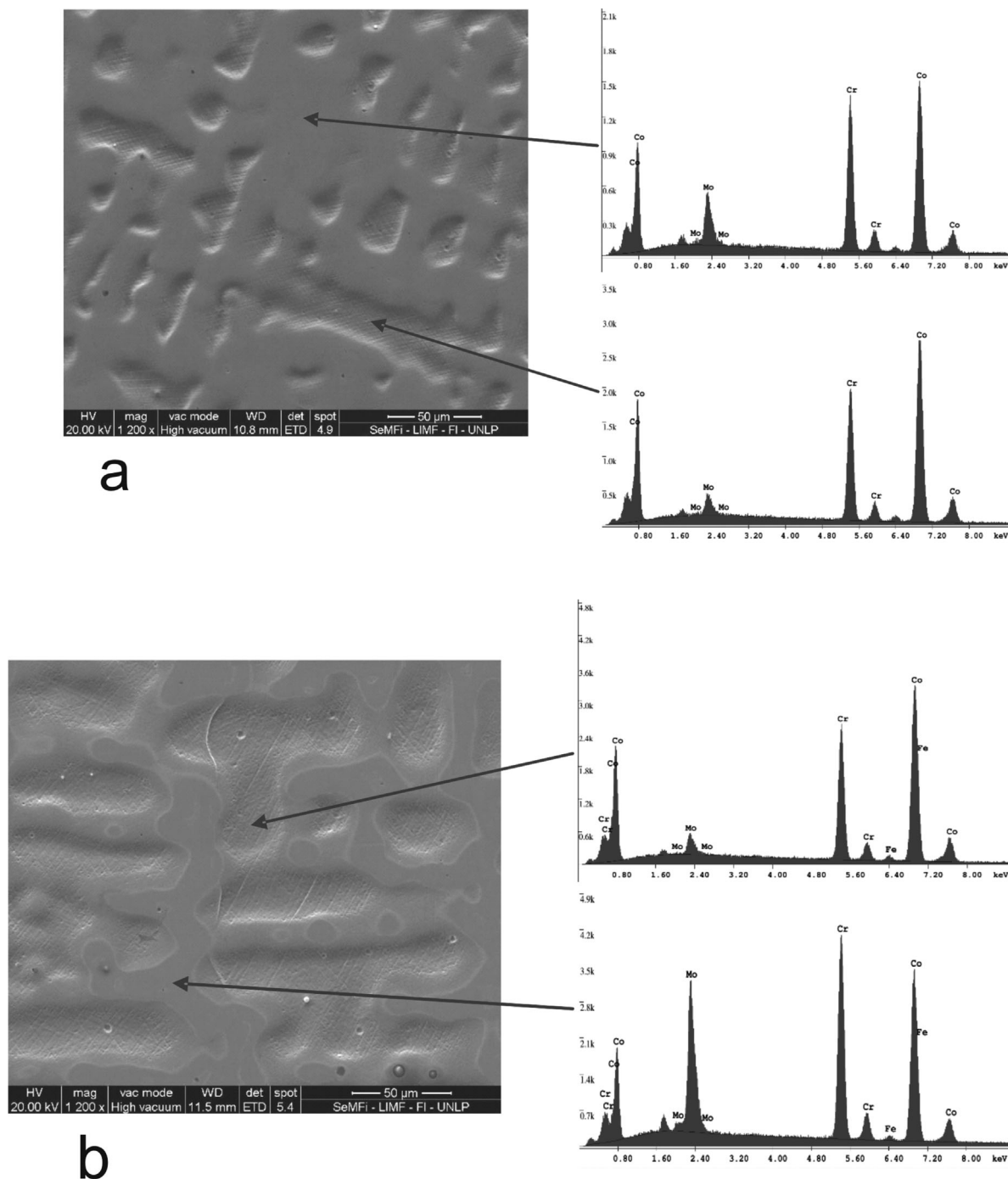
FIGURE 3 Microstructure and energy dispersive X-ray spectroscopy analysis in dendritic and interdendritic regions: (a) DR and (b) APR

density occurred at potentials ranging from 0.500 to 0.600 V/SCE. As pH increased, the passivity range decreased. At pH = 7, the increase in the anodic current density was observed at potentials between 0.250 and 0.300 V/SCE. At potentials between 0.350 and 0.400 V/SCE, the curve changed the slope, as a consequence of the beginning of transpassive reactions. In these two polarization curves, a narrow hysteresis loop was observed, a behavior characteristic of materials with high resistance to localized corrosion. The polarization curve performed at pH = 9 showed a peak at potentials close to

0.280 V/SCE, which would indicate the existence of a transpassive reaction. Then, the current density continued increasing from potentials close to 0.470 V/SCE, ending with a wide hysteresis loop. According to the common behaviour of high chromium materials, as stainless steels, transpassive reactions involves the oxidation of Cr^{+3} to Cr^{+6}, leading to the formation of soluble ions.[27]

To verify if the increase in the current density in the experiments at pH = 7 and pH = 9 was caused by localized corrosion or by a change in the oxidation state of chromium,

TABLE 2 Grain size and primary and secondary dendritic arm spacing of different regions of the samples

	Grain size (mm)	Primary dendritic arm spacing (µm)	Secondary dendritic arm spacing (µm)
DR	0.26	49.78	20.38
APR	1.15	58.15	38.2

the potentiodynamic–potentiostatic–potentiodynamic (PD–PS–PD) technique was performed. This technique has been used by other authors to determine the existence of localized corrosion in nickel–chromium–molybdenum alloys in bicarbonate solutions.[28] The scans were run at 0.500 V/SCE for pH = 7 solution and 0.300 V/SCE for pH = 9 solution. These potentials are slightly higher than those corresponding to the change of slope and peak of current density observed at those pH, respectively. In both tests, the potential was kept potentiostatically for 1 h. Then, it was scanned back to a potential lower than the potential at which the hysteresis loop is completed upon reverse polarization scan. The results are shown in Figure 6, where it can be seen that no positive hysteresis was observed, indicating the onset of localized corrosion. This result confirms that the increase in the anodic current density can be described by the change in the oxidation state of chromium, which leads to the formation of other soluble chromium oxides in the surface film. The polarization curves of Figures 4 and 5 show that the potential at which the oxidation change occurs decreases as pH increases, resulting in the reduction of the passive region. At the same time, the pH variation could promote the formation of other chromium oxides, according to the Pourbaix diagram in aqueous solutions[29] (Figure 7).

Although the thermodynamic conditions of the Pourbaix diagram are far from those exposed in the present work, it can serve as a reference to explain the behavior of the polarization curves obtained at the different pH values studied.

At pH = 5, the increase in the current density close to 0.550 V/SCE could be related to the change from Cr^{+3} to Cr^{+6}, according to the following reaction:

$$Cr_2O_3 + 5H_2O \rightarrow 2HCrO_4^- + 8H^+ + 6e^-. \quad (1)$$
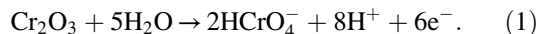
The curves corresponding to pH = 7 showed two increases in the current density. The first one could be attributed to the change in the oxidation state from Cr^{+3} to Cr^{+6} to form CrO_4^{-2}. According to Schmuki et al.,[30] the

TABLE 3 Concentration of elements in the bulk and interdendritic regions of the samples, in wt%

	APR			DR		
	Co	Cr	Mo	Co	Cr	Mo
Bulk	69.1	26.1	4.8	69.3	25.8	5.0
Interdendritic region	46.7	30.3	23.0	61.0	27.9	11.1
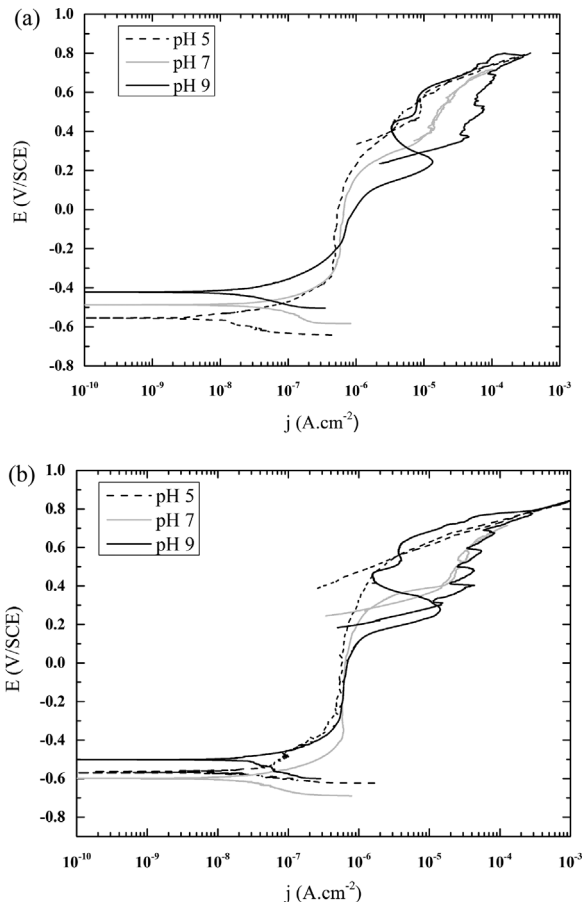
FIGURE 4 Polarization curves in a 0.9 wt% sodium chloride solution: (a) DR at 37 °C, (b) DR at 42 °C

CrO_4^{-2} formed is trapped by the passive film of Cr_2O_3 at first instance. Then, as the potential increases, it passes to the electrolytic solution, which is reflected by the second increase in current. This behavior is in accordance with previous research on transpassive dissolution of chromium oxide films.[31,32] As it is well known, the main component of the passive oxide film is chromium (about 90% chromium oxides). In previous works,[33–35] Milosev studied the composition of the oxide film in different solutions by X-ray photoelectron spectroscopy (XPS). In sodium chloride solution, as the case of the present work, the composition in the passive region is mainly composed of chromium oxide (Cr_2O_3) and chromium hydroxide [$Cr(OH)_3$], with lower content of cobalt and molybdenum oxides (CoO and MoO_3). In the transpassive region, the XPS analysis showed the presence of Cr^{+6} in the oxide layer. Milosev also suggested the formation of Co_2O_3/Co_3O_4 oxides, as a consequence of the change in the oxidation state of cobalt from Co^{+2} to Co^{+3}.

As mentioned above, the polarization curve corresponding to pH = 9 differs from those at pH 5 and 7, in that the transpassive region is more noticeable. The peak corresponding to the transpassive transformation occurred at potentials close to 0.280 V/SCE. At the same time, It was observed
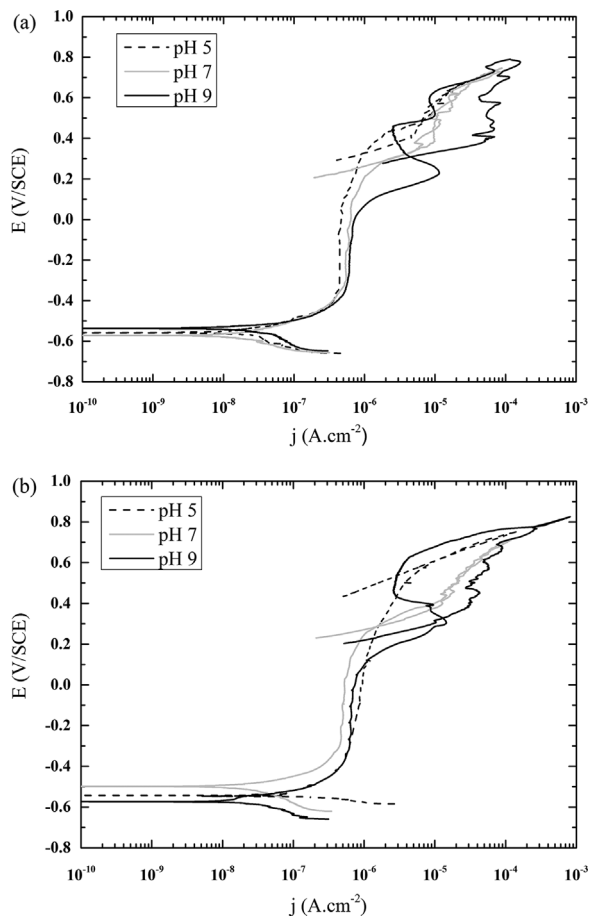
FIGURE 5 Polarization curves in a 0.9 wt% sodium chloride solution: (a) APR at 37 °C, (b) APR at 42 °C

another peak close to 0.490 V/SCE, which could be related to the change in the oxidation state of cobalt, as reported by other authors, who have stated that an increase in the current density at around 0.4 V (SCE) is also associated with the conversion of Co^{+2} to Co^{+3}.[36–38] Another relevant difference is the main hysteresis loop observed in this curve, which would indicate that at pH = 9, the material is more susceptibe to localized corrosion.

The microscopic analysis performed after the electrochemical tests, shown in Figure 8, revealed a surface pitting. This surface pitting developed mostly around non-metallic inclusions, which appear to be preferential sites for localized corrosion. This feature could be attributed to the decrease in the potential at which transpassive reactions, which are responsible for the formation of more soluble compounds, begin.

3.2.3 | Effect of temperature

The analysis of the temperature variation from 37 to 42 °C indicated no significant differences in the polarization curves. From the values reported in Table 4, it can be highlighted that E_{corr} shifted slightly toward lower potentials, while E_{ox} shifted to higher potentials at 42 °C. In accordance with these variations, the passivity range was slightly higher at 42 °C, for all the pH values analyzed.

In their tests on Nitinol and 316L stainless steel, Trépanier and Pelton[39] found that, as the temperature increased, the polarization curves shifted slightly towards more electronegative potentials. Their experiments were performed in a temperature range from 10 to 80 °C. In the present work, the temperature range studied (37–42 °C) was narrow to observe relevant changes in the polarization curves.

3.2.4 | Effect of the microstructure

The microstructure in the DR is finer, with smaller interdendritic spacing, and consequently, lower microsegregation than in the APR, Figure 3. The polarization curves revealed that in the sample corresponding to the APR, E_{corr} was lower than that of the DR. At the same time, E_{ox} and the passivity range were also smaller in the APR. Although these differences were not relevant, they lead to assume that the vastness of the microstructure would be detrimental to the resistance to localized corrosion. These results are in agreement with those of Hiromoto et al.[40] In their tests in cobalt-27chromium-6molybdenum alloys,

TABLE 4 Electrochemical parameters of cyclic potentiodynamic tests for the ASTM F75 alloy

| | | DR | | APR | |
	pH	*T* (37 °C)	*T* (42 °C)	*T* (37 °C)	*T* (42 °C)
E_{corr} (V)	5	−0.528 ± 0.080	−0.692 ± 0.169	−0.548 ± 0.149	−0.474 ± 0.072
	7	−0.525 ± 0.052	−0.583 ± 0.049	−0.563 ± 0.039	−0.575 ± 0.101
	9	−0.499 ± 0.072	−0.518 ± 0.020	−0.541 ± 0.030	−0.604 ± 0.035
E_{ox} (V)	5	0.360 ± 0.144	0.402 ± 0.126	0.462 ± 0.085	0.333 ± 0.153
	7	0.238 ± 0.031	0.260 ± 0.042	0.239 ± 0.036	0.276 ± 0.052
	9	0.107 ± 0.014	0.156 ± 0.104	0.099 ± 0.031	0.129 ± 0.046
E_{ox}–E_{corr} (V)	5	0.888 ± 0.144	1.090 ± 0.042	1.010 ± 0.098	0.807 ± 0.105
	7	0.764 ± 0.083	0.843 ± 0.080	0.801 ± 0.065	0.851 ± 0.147
	9	0.607 ± 0.086	0.675 ± 0.121	0.641 ± 0.060	0.733 ± 0.057
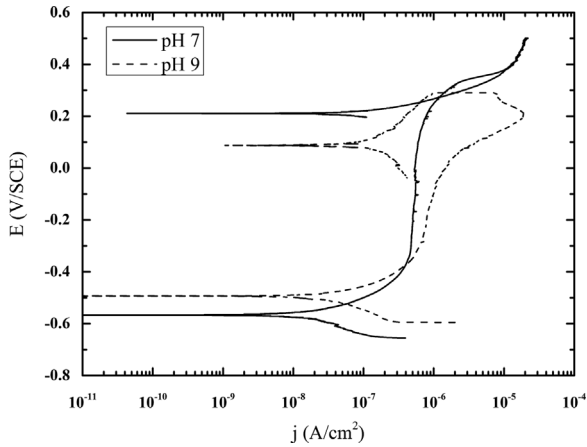
FIGURE 6 Potentiodynamic–potentiostatic–potentiodynamic (PD–PS–PD) curves obtained in a 0.9 wt% NaCl solution at pH = 7 and pH = 9

FIGURE 8 Surface image of the APR tested at pH = 9

these authors found that the OCP in Co-based alloys with larger grain size is slightly lower than that of the same alloys with smaller grain size. These authors concluded that the increase in grain boundaries with grain refining leads to the increase in anodic reaction and causes the negative shift of the OCP.

3.2.5 | EIS results

EIS allows determining the kinetic processes in the passive film, in addition to its thickness, dielectric constant, and diffusion coefficient. It also allows analyzing changes in the passive film caused by variations in test conditions, such as temperature, electrolyte composition, and pH.[41]

Experimental data were fitted according to the equivalent electrical circuits shown in Figure 9, where R_u represents the electrolyte resistance.
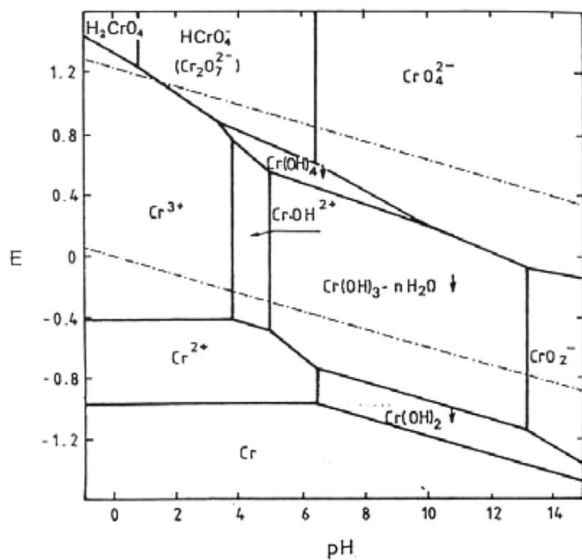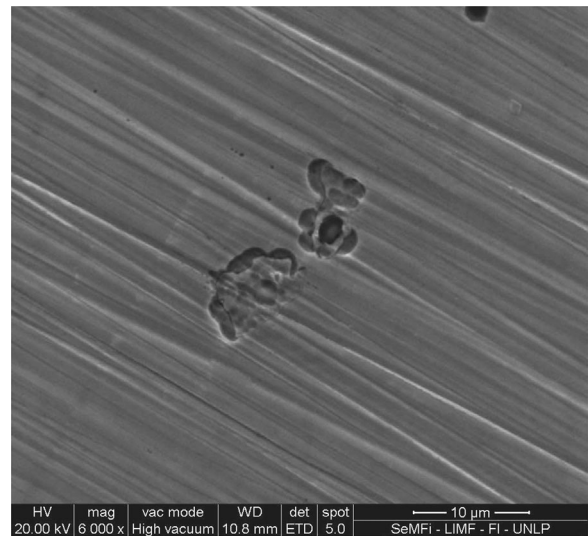
In the electrolyte/passive film interface, a double layer capacitance (C_{dl}) occurs, which is represented by a combination of a constant phase element (Q_t) and the resistance to charge transfer (R_t). The passive film is represented by a constant phase element, (Q_{ox}), with resistance R_{ox}. Both Q_t and Q_{ox} represent C_{dl} and the capacitance of the passive film respectively when they are ideal capacitances, i.e., when the identity coefficients n_t and n_{ox} are close to 1.

The constant phase element is introduced because of the roughness, impurities, dislocations, or grain boundaries on the surface. These inhomogeneities are presented at the microscopic level under the oxide and the electrolyte/passive film interface. The relationship for the impedance of a
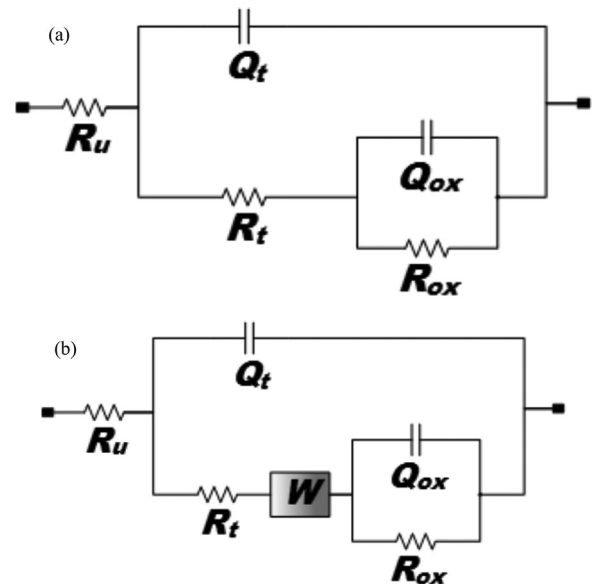

FIGURE 7 Pourbaix diagram of chromium

FIGURE 9 Equivalent circuit in a 0.9 wt% NaCl solution. (a) pH 5 and 7, (b) pH 9

TABLE 5 Electrochemical parameters of EIS tests for the ASTM F75 alloy

		DR		APR	
	pH	T (37ºC)	T (42ºC)	T (37ºC)	T (42ºC)
R_p $(\Omega \cdot cm^2)$	5	3.35E + 05	1.15E + 05	4.18E + 04	4.30E + 05
	7	3.37E + 05	1.99E + 04	2.46E + 05	3.15E + 05
	9	7.96E + 05	2.94E + 05	2.85E + 04	3.34E + 04
Q_t $(\Omega^{-1} cm^2 s^n)$	5	4.25E − 05	3.66E − 05	4.18E − 05	4.31E − 05
	7	2.80E − 05	1.25E − 05	2.74E − 05	2.49E − 05
	9	2.98E − 05	2.33E − 05	1.63E − 05	3.40E − 05
n_t	5	0.887	0.860	0.895	0.890
	7	0.907	0.940	0.882	0.892
	9	0.919	0.890	0.907	0.902
Q_{ox} $(\Omega^{-1} cm^2 s^n)$	5	8.29E − 05	1.74E − 04	6.42E − 05	8.33E − 05
	7	7.37E − 05	6.93E − 06	3.60E − 04	3.77E − 05
	9	2.50E − 05	1.11E − 05	2.53E − 05	1.28E − 05
n_{ox}	5	0.810	0.812	0.703	0.792
	7	1.00	0.892	1.00	1.00
	9	0.950	0.853	1.00	1.00
R_{ox} $(\Omega \cdot cm^2)$	5	3.27E + 06	2.31E + 06	1.05E + 06	7.34E + 05
	7	1.66E + 05	1.95E + 06	1.39E + 05	8.50E + 05
	9	1.34E + 06	1.71E + 07	3.25E + 05	2.74E + 05

constant phase element is as follows:

$$Z = \frac{1}{Q(i\omega)^n} \quad (2)$$

where Q and n are independent parameters, $n = 1$ represents a capacitor, $n = 0.5$ represents a Warburg element (W), $n = 0$ represents a resistance, and $n = -1$ represents an inductor.

The element W represents the unidirectional diffusion through the double layer, which can be related to the diffusion of the oxygen dissolved in the electrolyte. The values of the parameters obtained from the fitting are listed in Table 5.

3.2.6 | Effect of pH

Figure 10 shows the equivalent circuit models for the three pH values analyzed.

At pH = 5, the equivalent circuit modeling the experimental data was observed to be composed of two parallel elements RQ, which describe the behavior of the electrical double layer and the passive film. In contrast, when the pH was increased up to a neutral value, the equivalent circuit experienced some changes. The new model representing the experimental data was composed of two elements: an RQ, representing the electrical double layer, and RC, showing that the passive film has a pure capacitive behavior. At basic pH, the new equivalent circuit incorporates a Warburg element

representing the dimensional diffusion of charged species through the double layer.

The polarization resistance (R_p), defined as the sum of R_t and R_{ox}, increased with increasing pH in the DR, because of the decrease in the dissolution rate of the passive film. The behavior in the APR was opposite, revealing that R_p decreases as pH increases. The constant phase element decreased with increasing pH. This may involve a decrease in the amount of charges present on the electrical double layer. On the other hand, the coefficient n_t associated with the constant phase element showed, in most cases, a tendency to increase with increasing pH. This suggests that the passive layer becomes more compact and, in some cases, behaves as a pure capacitor. At the same time, it could indicate that ions are more ordered in the electrical double layer.

The analysis of the constant phase element, which represents the passive film, revealed that the capacitance decreases with increasing pH. This feature can be related to the increase in the passive film thickness, which, according to Eq. (3), is inversely proportional to the capacitance. Finally, R_{ox} showed no tendency with increasing pH.

As a summary of the effect of pH on the EIS results, it should be highlighted that as pH increases, the passive film becomes more compact and thicker. These results are in agreement with those obtained in CPT, which showed that the corrosion potential is displaced towards slightly more anodic potentials as pH increases. However, impedance tests showed a random behavior of the resistors present on
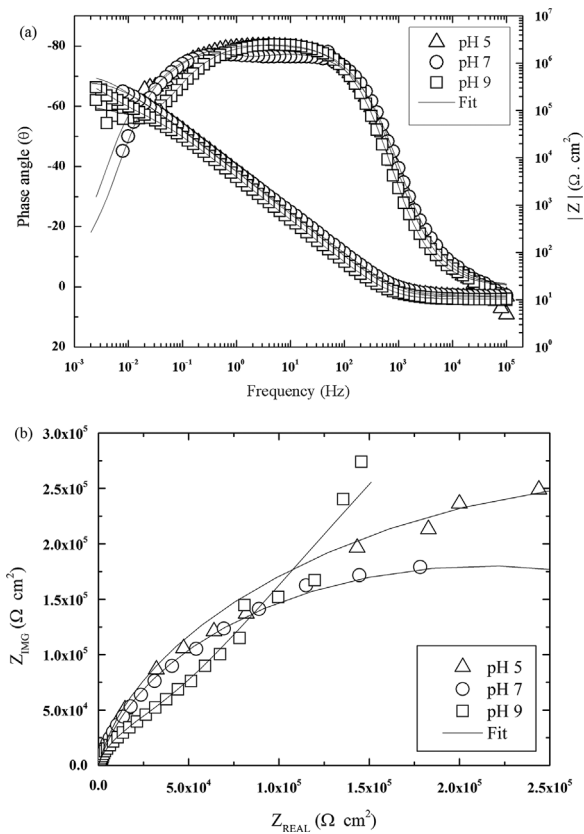
FIGURE 10 Effect of pH in a 0.9 wt% NaCl solution. (a) Bode plot. (b) Nyquist diagram

became neutral or basic. The capacitance is directly proportional to the dielectric constant of the oxide ε and inversely proportional to the thickness of the passive film d, as follows[42]:

$$C = \frac{\varepsilon \varepsilon_o A}{d} \qquad (3)$$

where ε_o is the dielectric permittivity in the vacuum and A is the effective surface region.

The coefficient n associated with the constant phase elements showed a tendency to increase with temperature at pH = 5, indicating that the passive layer becomes more compact. At neutral and basic pH, n_{ox} decreased with temperature in the APR, which indicates that, in this case, the passive layer is less compact. In the APR, the passive film behaves as a pure capacitor.

The resistance R_{ox} decreased with increasing temperature at pH = 5, in response to a higher dissolution rate, in coincidence with the results obtained by Valero Vidal et al.[41] In contrast, at pH = 7, R_{ox} increased with temperature, while at pH = 9 no definite tendency was observed.

Figure 11 shows that the phase angle curve shifts to higher frequencies with increasing temperature and the impedance module at lower frequencies. Thus, it can be highlighted that
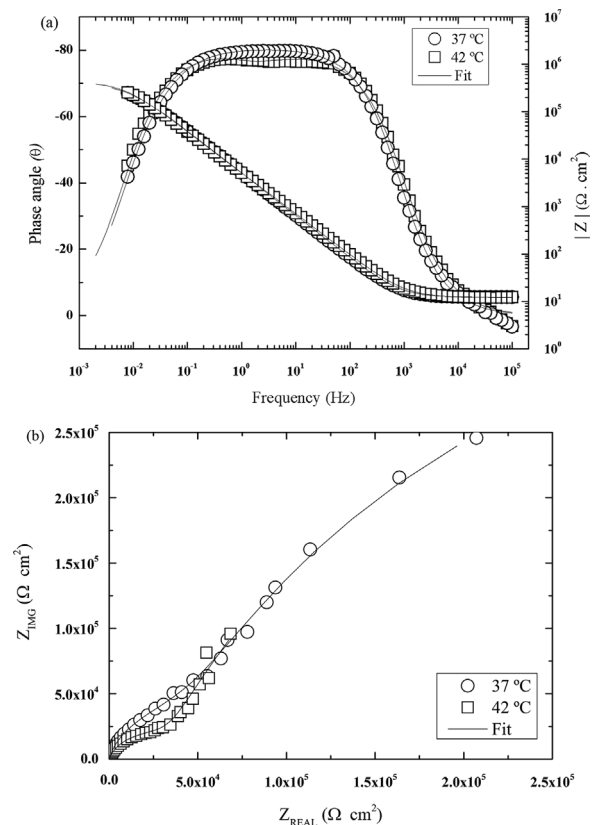
the surface by increasing the pH of the electrolyte, making it difficult to find a relationship between the CPT and EIS tests.

3.2.7 | Effect of temperature

R_p decreased as temperature increased in the DR. This variation was due to the increase in the dissolution rate of the passive film in that region. In contrast, R_p increased with temperature in the APR.

The constant phase element, associated with the electrical double layer, decreased as the temperature increased in the DR, which could be attributed to the decrease in the charges present on the electrical double layer. Conversely, in the APR, the capacitance increased with temperature because of the increase in the charges on that layer. On the other hand, the coefficient n associated with the constant phase element decreased as the temperature increased. This feature was manifested as an increase in the disorder of ions in the electrical double layer, which led to a greater diffusion of charges into the electrolyte/passive film interface. This behavior was observed for all the pH values evaluated, except for pH = 7.

Regarding the constant phase element, associated with the oxide, the capacitance increased with temperature at acid pH, while it decreased with temperature when pH

FIGURE 11 Effect of temperature in a 0.9 wt% NaCl solution. (a) Bode plot. (b) Nyquist diagram

as temperature increases, the passive film becomes less compact in the DR. These results are in agreement with those obtained in CPT, which showed that the corrosion potential is displaced towards slightly more cathodic potentials as temperature increases.

4 | CONCLUSIONS

The ASTM F75 alloy showed a decrease in the passivity of the chromium oxide film in sodium chloride solutions at increasing pH values. It could be inferred that the decrease in passivity is caused by transpassive reactions that promote the formation of soluble CrO_4^{-2} ions. The transpassivity was more noticeable in the samples tested at pH = 9, in which also evidence of localized corrosion was observed. The mechanism by which the passive chromium oxide film is dissolved would be that the resistance of the film decreases with increasing pH, promoting the diffusion of charged species. Finally, neither the variation in the microstructure nor that in temperature showed significant effects on the electrochemical behavior of the alloy.

REFERENCES

[1] A. C. Fraker, *Corrosion*, ASM International, Materials Park OH **1992**.

[2] G. Manivasagam, D. Dhinasekaran, A. Rajamanickam, *Recent Patents on Corrosion Science* **2010**, *2*, 40–54.

[3] D. C. Hansen, *The Electrochemical Society Interface* **2008**, *17*, 31.

[4] Q. Chen, G. A. Thouas, *Mat. Sci. Eng. R* **2015**, *87*, 1.

[5] T. Hanawa, *Mater. Sci. Eng. C* **2004**, *24*, 745.

[6] J. B. Brunski, *Biomaterials Science – An Introduction to Materials in Medicine*, Elsevier Academic Press, California **2004**.

[7] H. Hermawan, D. Ramdan, J. R. P. Djuansjah, http://www.intechopen.com/books/biomedical-engineering-from-theory-toapplications/metals-for-biomedical-applications. accessed: October, **2016**.

[8] R. W. Gregorutti, J. E. Grau, C. I. Elsner, *Mater. Sci. Tech. Ser.* **2012**, *28*, 742.

[9] P. Kapranos, C. Carney, A. Pola, M. Jolly, *Compr. Mater. Process.* **2014**, *5*, 39.

[10] S Pattnaik, D Benny Karunakar, P. K Jha, *J. Mater. Process Tech.* **2012**, *212*, 2332.

[11] A. Marti, *Int. J. Care Injured* **2000**, *31*, S-D18.

[12] B. Patel, G. Favaro, F. Inam, M. J. Reece, A. Angadji, W. Bonfield, J. Huang, M. Edirisinghe, *Mater. Sci. Eng. C* **2012**, *32*, 1222.

[13] *ASTM F75-0*, ASTM International, Conshohocken, Section 13, **2001**.

[14] R. Kaiser, K. Williamson, C. O'Brien, S. Ramirez-Garcia, D. J. Browne, *J. Mech. Behav. Biomed. Mater.* **2013**, *24*, 53.

[15] R. Kaiser, K. Williamson, C. O'Brien, D. J. Browne, *Metall. Mater. Trans. A* **2013**, *44*, 5333.

[16] S. H. Teoh, *Int. J. Fatigue* **2000**, *22*, 825.

[17] K. V. Sudhakar, *Eng. Fail. Anal.* **2005**, *12*, 249.

[18] K. D. Ralston, N. Birbilis, C. H. J. Davies, *Scripta Mater.* **2010**, *63*, 1201.

[19] K. D. Ralston, D. Fabijanic, N. Birbilis, *Electrochim. Acta* **2011**, *56*, 1729.

[20] S. Gollapudi, *Corros. Sci.* **2012**, *62*, 90.

[21] W. R. Osorio, C. M. Freire, A. Garcia, *Mat. Sci. Eng. A* **2005**, *402*, 22.

[22] W. R. Osorio, C. M. Freire, A. Garcia, *J. Alloy Compd.* **2005**, *397*, 179.

[23] K. D. Ralston, N. Birbilis, *Corrosion* **2010**, *66*, 075005–075001.

[24] A. I. Kociubczyk, C. M. Méndez, R. W. Gregorutti, A. E. Ares, *Procedia Mater. Sci.* **2015**, *9*, 335.

[25] H. R. Lashgari, Sh. Zangeneh, F. Hasanabadi, M. Saghafi, *Mat. Sci. Eng. A* **2010**, *527*, 4082.

[26] T. Narushima, S. Mineta, Y. Kurihara, K. Ueda, *JOM-J. Min. Met. Mat. S.* **2013**, *65*, 489.

[27] D. W. Shoesmith, *Corrosion: Fundamentals, Testing, and Protection. Vol 13A, ASM Handbook*, ASM International, Materials Park **2003**, pp. 42–51.

[28] A. K. Mishra, S. Ramamurthy, M. Biesinger, D. W. Shoesmith, *Electrochim. Acta* **2013**, *100*, 118.

[29] M. Pourbaix, *Atlas of Electrochemical Equilibria in Aqueous Solutions*, NACE, Houston, TX **1974**, pp. 257–329.

[30] P. Schmuki, S. Virtanen, A. J. Davenport, C. M. Vitus, *J. Electrochem. Soc.* **1996**, *143*, 3997.

[31] A. W. E. Hodgson, S. Kurz, S. Virtanen, V. Fervel, C.-O. A. Olsson, S. Mischler, *Electrochim. Acta* **2004**, *49*, 2167.

[32] B. G. Pound, *J. Biomed. Mater. Res. A* **2010**, *94*, 93.

[33] V. S. Saji, H. Choe, *T. Nonferr. Metal Soc.* **2009**, *19*, 785.

[34] I. Milosev, H. H. Strehblow, *Electrochim. Acta* **2003**, *48*, 2767.

[35] I. Milosev, *Electrochim. Acta* **2012**, *78*, 259.

[36] B. G. Pound, *J. Biomed. Mater. Res. A* **2014**, *102*, 1595.

[37] A. Kocijan, I. Milosev, B. Pihlar, *J. Mater. Sci-Mater. M.* **2004**, *15*, 643.

[38] M. Behazin, M. C. Biesinger, J. J. Noël, J. C. Wren, *Corros. Sci.* **2012**, *63*, 40.

[39] C. Trépanier, A. R. Pelton, presented at *Proceedings of ASM Materials and Processes for Medical Devices Conference*, 24–27 August, **2004**, pp. 392–397.

[40] S. Hiromoto, *Biomaterials* **2005**, *26*, 4912.

[41] C. Valero Vidal, A. Igual Muñoz, http://www.intechopen.com/books/biomedical-engineering-trends-in-materials-science/electro chemical-aspects-in-biomedical-alloy-characterization-electro chemical-impedance-spectrosopy, accessed: October, 2016.

[42] J. Cassar, B. Mallia, A. Karl, J. Buhagiar, *Surf. Coat. Tech.* **2016**, *292*, 90.